

Simple Model for a Distributed Feedback Laser Integrated With a Mach–Zehnder Modulator

S. F. Yu and N. Q. Ngo, *Member, IEEE*

Abstract—This paper presents a time-domain traveling-wave algorithm for the modeling of the large-signal dynamic response of a distributed feedback laser integrated with a Mach–Zehnder (MZ) modulator. The influence of residual optical feedback from the output of the modulator facet on the dynamic frequency chirp is studied. It is found that the difference in frequency chirp between the turn-on and -off states (i.e., adiabatic chirp) of a $\pi/2$ -shifted 2×2 MZ modulator is minimal and is independent of the residual optical feedback. In addition, it can be shown that the presence of chirped frequency spikes (i.e., transient chirp), due to the change in refractive index as a result of the rapid variation of the bias voltage, can broaden the linewidth and distort the spectrum of the modulated optical signal. Furthermore, the possibility of doubling the modulation frequency of MZ modulators using a dual-arm dual-signal modulation format is investigated.

Index Terms—Distributed feedback lasers, frequency chirp, large-signal modulation, Mach–Zehnder modulators, monolithic integration, numerical simulation, optical feedback.

I. INTRODUCTION

A DISTRIBUTED feedback (DFB) laser integrated with a multiple-quantum-well (MQW) p-i-n waveguide Mach–Zehnder (MZ) modulator has important applications in high-speed long-haul optical fiber communication systems [1], [2]. This is because with a suitable design of the electrooptic properties of the p-i-n waveguide [3], the splitting ratios of the two Y-junctions [4], the differential phase shift between the two arms [5] as well as the format of the modulation scheme [6], and low-frequency chirp at high modulation speeds can be realized. In fact, it has been demonstrated that a DFB laser integrated with an MZ modulator exhibits a high transmission speed (>10 Gb/s) over a long transmission distance (>80 km) in a nondispersion-shifted fiber [1], [2].

The static and dynamic responses of a DFB laser integrated with an MZ modulator have been modeled using various techniques [7]–[9]. For example, an equivalent circuit model is developed to analyze the steady-state response of an MZ modulator [7]. In the model, the variation of attenuation and phase constants under the influence of bias voltage is deduced experimentally and fitted empirically to the model. This model is relatively simple but has ignored the physical characteristics of the MZ modulator. Hence, a detailed physical model has been developed to analyze the frequency chirp of a 2×1 MZ modulator integrated with a DFB laser using the transfer matrix

method [8]. Detailed information concerning the Y-junction, the mode converter at the interface of the junctions, as well as the MZ modulator have been taken into consideration using an appropriate transfer matrix. This model can simulate a more realistic structure of a MZ modulator with fewer approximations [8]. However, this model is only limited to the calculation of the adiabatic frequency chirp but not the transient response of the devices. On the other hand, transfer matrix and time-dependent rate equations have been used to model the dynamic response of MZ modulators [9]. But the model is restricted to the analysis of a small-signal response [i.e., amplitude modulation (AM) and frequency modulation (FM) responses] of MZ modulators. However, the large-signal dynamic response of a DFB laser integrated with an MZ modulator has not been investigated previously.

It must be noted that the optical output of the MZ modulators under large-signal modulation always exhibits chirped frequency spikes (i.e., transient chirp). Although the chirped frequency spikes are only a small percentage of the total spectral energy of the frequency chirp response [10], the presence of the chirped frequency spikes may broaden and distort the modulated optical signal. Therefore, it is useful to have a simple model that can be used to analyze the large-signal dynamic response of MZ modulators with the effect of residual optical feedback taken into consideration.

In this paper, a simple and versatile model for a DFB laser integrated with an MZ modulator is developed using a time-domain traveling-wave algorithm [10]. Using this model, the static and dynamic responses of MZ modulators with 2×1 and 2×2 multimode interference (MMI) couplers are studied. It is shown that the time-domain algorithm is the simplest, and yet powerful, method for the self-consistent study of the large-signal dynamic response of a DFB laser integrated with an MZ modulator. This paper is organized as follows. In Section II, a model for a DFB laser integrated with an MZ modulator is developed using the time-domain algorithm. In Section III, the steady-state, AM, and FM responses of a DFB laser integrated with an MZ modulator with an asymmetric 2×1 MMI coupler are calculated and verified to demonstrate the effectiveness of the proposed time-domain algorithm. In addition, the corresponding frequency chirp response (i.e., including chirped frequency spikes and frequency chirp at turn-on and -off states) under large-signal modulation is studied. Furthermore, the frequency chirp response of MZ modulator with a $\pi/2$ shifted 2×2 MMI coupler is analyzed by taking residual optical feedback into account. It can be shown that the difference in frequency chirp between turn-on and -off states of the 2×2 MZ modulator is minimal and is independent of the residual optical

Manuscript received December 19, 2001; revised April 11, 2002.

The authors are with the School of Electrical and Electronic Engineering, Nanyang Technological University, Singapore 639798 (e-mail: esfyu@ntu.edu.sg).

Publisher Item Identifier 10.1109/JQE.2002.800996.

feedback. It is also noted that the presence of chirped frequency spikes can broaden and distort the spectrum of the modulated optical signal. Furthermore, the possibility of using a dual-arm dual-signal modulation format to double the modulation speed of an MZ modulator is studied. The conclusions are given in Section IV.

II. THEORETICAL MODEL

Fig. 1 shows the schematics of the integrated laser-MZ modulators. The laser is assumed to be a single-mode $1.56\text{-}\mu\text{m}$ $2 \times \lambda/8$ InP MQW DFB laser. Two configurations of MZ modulators are considered in this analysis: 1) an MZ modulator with a 2×1 MMI output coupler (i.e., both arms of the MZ are coupled to a unique output waveguide) and 2) an MZ modulator with a 2×2 MMI output coupler (i.e., both arms of the MZ are coupled to two output waveguides). In addition, it is assumed that the MMI couplers have a coupling ratio of 50 : 50. In Fig. 1, L is the length of the DFB laser, L_{WG1} is the waveguide section connecting the laser section and the Y-splitter junction of the MZ modulator, L_{MZ} is the length of both arms of the MZ modulator, and L_{WG2} is the waveguide section connecting the output Y-combiner junction of the MZ modulator to the output coupler (i.e., 2×1 or 2×2 output coupler). It must be noted that the optical length of both arms of the MZ modulator is assumed to be identical in the calculation but the actual physical length can vary with the appropriate adjustment of the relative optical absorption loss and phase between both arms. Three types of MZ modulators will be considered in the following analysis, namely: 1) symmetric 2×1 with both arms in-phase; 2) an asymmetric 2×1 with a π phase-shift between both arms; and 3) 2×2 with $\pi/2$ phase-shifted between both arms. Furthermore, optical absorption and refractive index (i.e., phase) of arm A (as well as arm B) of the MZ modulator section are controlled by the reverse bias voltage.

A. Time-Dependent Coupled Wave Equations

Several theoretical models have been developed to analyze the static and dynamic responses of a laser-modulator such as those using the transmission line method [11], the transfer matrix method [12], [13], and the time-domain traveling-wave method [14]. It has been shown that the use of time-domain traveling-wave algorithm to model the dynamic performance of an integrated laser-electro-absorption modulator [10] is the simplest approach when compared with other methods [7]–[9]. It will be shown in this paper that the static and dynamic responses of an integrated laser-MZ modulator can be easily modeled using the same time-domain traveling-wave algorithm. The model can be implemented by solving the coupled wave equation as given [14]

$$\left(\frac{1}{\nu_g} \frac{\partial}{\partial t} + \frac{\partial}{\partial z}\right) F_i = \left(\frac{1}{2}\Gamma g + j\Delta\beta\right) F_i + jkR_i + U_f \quad (1a)$$

$$\left(\frac{1}{\nu_g} \frac{\partial}{\partial t} - \frac{\partial}{\partial z}\right) R_i = \left(\frac{1}{2}\Gamma g + j\Delta\beta\right) R_i + jkF_i + U_r \quad (1b)$$

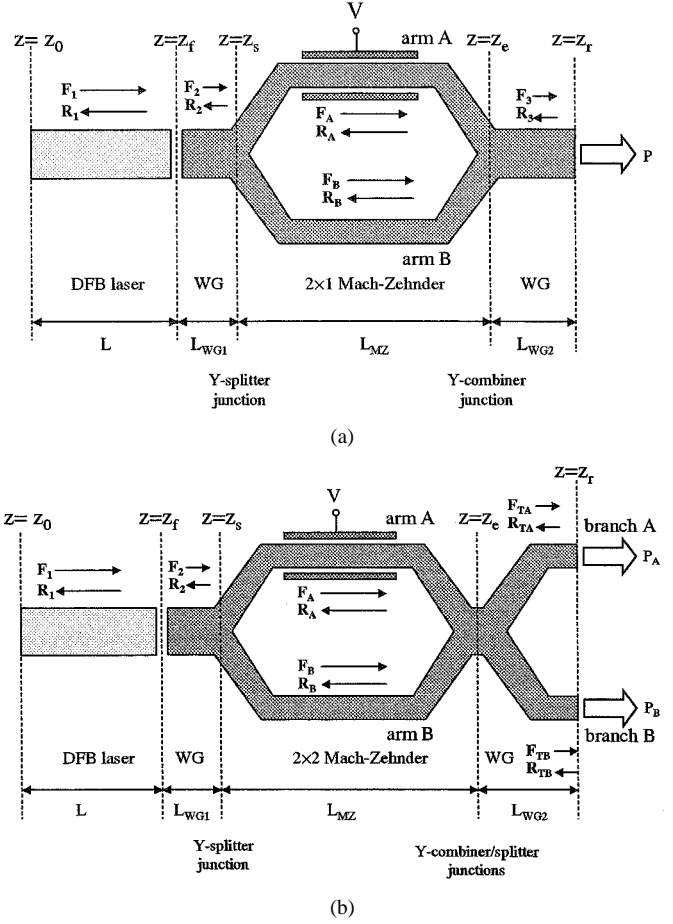


Fig. 1. Schematic configurations of (a) a laser integrated with an MZ modulator with a 2×1 MMI output coupler and (b) a laser integrated with an MZ modulator with a 2×2 MMI output coupler.

where $j = \sqrt{-1}$, ν_g is the group velocity, Γ is the transverse confinement factor, and F_i and R_i are, respectively, the forward and reverse optical fields propagating along the longitudinal direction z and also varying in time t . The subscript i represents the optical fields propagating inside the laser section ($i = 1$), waveguide section ($i = 2$), arms of the MZ modulator ($i = A$ and B), as well as inside the output coupler section ($i = 3$, also denoted TA and TB). The notation of the optical fields inside the integrated laser-MZ modulator is also shown in Fig. 1.

In order to take into consideration the laser, waveguide, and MZ modulator sections of the integrated device, the parameter g given in (1) is expressed as

$$g = \begin{cases} a_N \log(N/N_t)/(1 + \varepsilon S) - \alpha_c, & \text{laser section} \\ -\alpha_c, & \text{waveguide section} \\ -\alpha_{\text{MZ}}(\lambda_R, V), & \text{MZ section} \end{cases} \quad (2)$$

where a_N is the gain coefficient, N_t is the carrier concentration at transparency, N is the injection carrier concentration, ε is the gain compression factor, α_c is the free carrier absorption and scattering losses, and $S (= |F_1|^2 + |R_1|^2)$ is the photon density inside the laser cavity. Hence, the expression $a_N \log(N/N_t)/(1 + \varepsilon S) - \alpha_c$ represents the net optical gain, which is a function of the injected carrier concentration inside the MQW active layer of the DFB laser. The term $-\alpha_c$, which is a material-dependent parameter, is considered to be the

effective waveguide loss. α_{MZ} is the electro-absorption loss of arm- A or - B of the MZ modulator, which is a function of the reverse bias voltage V being applied to the arm of the modulator as well as the resonant wavelength λ_R .

The parameter k given in (1) can be expressed as

$$k = \begin{cases} \kappa, & \text{laser section} \\ 0, & \text{waveguide/MZ section} \end{cases} \quad (3)$$

where κ is the coupling coefficient, which couples the forward and reverse propagating waves along the longitudinal direction. In (3), it is assumed that the coupling of the forward and reverse fields only occurs inside the DFB laser.

U_f and U_r are the forward and reverse spontaneous emission noises coupled to the forward and reverse optical fields, respectively. These spontaneous emission noises are assumed to have the same amplitude and are generated from a Gaussian distributed random number generator [14] that satisfies the following correlation:

$$\begin{aligned} \langle U_i(z, t) U_i^*(z', t') \rangle &= \beta_s K B_{\text{sp}} N^2 \delta(t - t') \delta(z - z') / \nu_g \\ \langle U_i(z, t) U_i(z', t') \rangle &= 0 \end{aligned} \quad (4)$$

where β_s is the spontaneous emission factor, K ($=1$) is the Petermann constant, B_{sp} is the bimolecular carrier coefficient, and δ is the delta function. It must be noted that the spontaneous emission noise is only coupled to the forward and reverse fields inside the laser section and is assumed to be zero in the other sections.

$\Delta\beta$ given in (1) represents the phase change of the forward and reverse fields and inside the laser, waveguide, and MZ modulator is given by

$$\Delta\beta = \begin{cases} 2\pi \cdot \Delta n_L(\lambda_R, N) / \lambda_R, & \text{laser section} \\ 0, & \text{waveguide section} \\ 2\pi \cdot \Delta n_{\text{MZ}}(\lambda_R, V) / \lambda_R, & \text{MZ section.} \end{cases} \quad (5)$$

In (5), the top expression of $\Delta\beta$ is related to the small change of the effective refractive index, Δn_L , inside the active region of the laser section. Hence, Δn_L can be expressed in terms of the injected carrier concentration by the following equation:

$$\Delta n_L = -\Gamma \alpha_H \frac{\lambda_R}{4\pi} \frac{a_n}{N} \Delta N \quad (6)$$

where α_H represents the linewidth enhancement factor and ΔN is the change of injected carrier concentration, N . Therefore, $\Delta\beta$ in the laser section can be interpreted as the shift of wavelength from the Bragg wavelength. The middle expression for $\Delta\beta$ in (5) is set to zero inside the waveguide section because it is assumed that the optical fields inside the laser and waveguide sections are phase-matched. The bottom expression for $\Delta\beta$ in (5) represents the change of phase of the optical fields inside the arms of the MZ modulator due to the electrooptical effect and Δn_{MZ} is the corresponding change of the refractive index due to the reverse bias voltage V . Hence, (2)–(6) can be considered as the auxiliary equations to model the optical fields propagating along the laser, waveguide, and MZ modulator sections.

B. Electrical Equations for the Laser and Modulator Sections

Inside the laser section, the amplification of optical power is directly related to the amount of injected carrier concentration, which can be deduced from the rate equation for the carrier concentration N , as shown below [14]:

$$\frac{\partial N}{\partial t} = \frac{J}{qd} - \frac{N}{\tau_n} - B_{\text{sp}} N^2 - \nu_g \frac{a_N \log(N/N_t)}{1 + \epsilon S} S \quad (7)$$

where J is the injection current density, q is the electron charge, d is the thickness of the MQW active layer, and τ_n is the carrier lifetime. Hence, the terms N/τ_n and $B_{\text{sp}} N^2$ denote the loss of carrier concentration due to nonradiative and radiative recombination, respectively, of carriers inside the MQW active region. It must be noted that N represents the longitudinal distribution of carrier concentration along the z direction of the laser section.

It is assumed that the MZ modulator operating at $1.56 \mu\text{m}$ is an InP-based MQW waveguide. Hence, the variation of α_{MZ} , $\Delta\alpha_{\text{MZ}}$, from its minimum reverse bias voltage (i.e., $V = 0.5 \text{ V}$) to a reverse bias voltage V (< 5.0) can be expressed by [9]

$$\Delta\alpha_{\text{MZ}}(V) = 0.248 \exp(V) - 0.270V + 0.040V^2 \quad (8a)$$

where, at zero bias, $\alpha_{\text{MZ}} = 2.1 \text{ cm}^{-1}$. It is noted that the change of $\Delta\beta$ due to reverse bias voltage can be expressed in terms of the total phase change between both arms of the MZ modulator, $\Delta\phi_{\text{MZ}} (= \Delta\beta \times L_{\text{MZ}})$. Again, using the empirical fitted curve obtained from [9], $\Delta\beta$ can be obtained from the expression of $\Delta\phi_{\text{MZ}}$, which is given by

$$\Delta\phi_{\text{MZ}}(V) = 0.027 + 0.265V + 0.108V^2. \quad (8b)$$

In order to analyze different types of MZ modulators, a phase shift of π must be added to (8b) to model the MZ modulator with an asymmetric 2×1 MMI coupler, and a phase shift of $\pi/2$ must also be added to (8b) to model an MZ modulator with a 2×2 MMI coupler.

The static and dynamic responses of the laser-MZ modulator can be calculated by solving (1) and (7) simultaneously. However, knowledge of the auxiliary equations is not enough to solve the coupled wave equations because the boundary conditions have to be defined for the traveling waves at the interfaces between the laser, waveguide, and MZ modulator sections.

C. Boundary Conditions for the Traveling Waves

Referring to Fig. 1, the boundary conditions for the forward and reverse fields, F_1 and R_1 , at the left facet of the DFB laser (i.e., $z = z_0$) can be written as

$$F_1(z_0, t) = r_L R_1(z_0, t) \quad (9)$$

where $r_L (= |r_L| \exp(j\phi_L))$ is the left facet reflectivity of the DFB laser and ϕ_L is the corresponding facet phase. At the interface between the right end facet of the DFB laser and the input of the MZ modulator (i.e., $z = z_f$), the forward and reverse fields, F_1 and R_1 as well as F_2 and R_2 , are related using the scattering matrix as follows:

$$\begin{bmatrix} F_2(z_f, t) \\ R_1(z_f, t) \end{bmatrix} = \begin{bmatrix} t_{LM} & -r_{LM} \\ r_{LM} & t_{LM} \end{bmatrix} \begin{bmatrix} F_1(z_f, t) \\ R_2(z_f, t) \end{bmatrix} \quad (10)$$

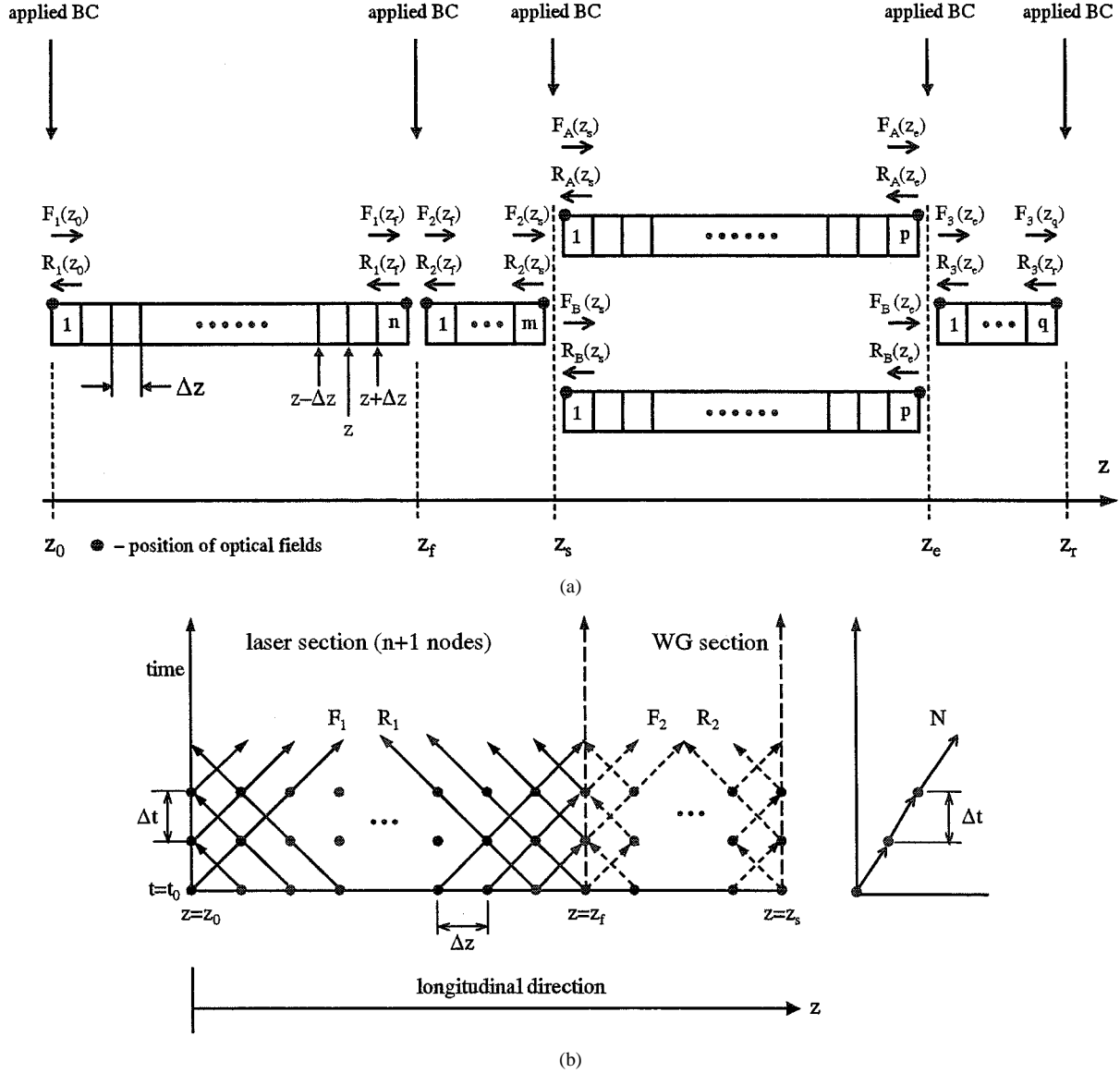


Fig. 2. (a) Implementation of a laser integrated with an MZ modulator with a 2×1 MMI output coupler using the proposed algorithm. (b) Explanation of the time-domain traveling-wave calculation method for the optical fields and carrier concentration.

where r_{LM} and t_{LM} are the field reflection and transmission coefficients, respectively, between the laser and waveguide sections, and $t_{LM} = \sqrt{1 - r_{LM}^2}$ has been used in (10).

At the first Y-splitter junction of the MZ modulator, we assign $z = z_s$. The forward and reverse fields F_2 and R_2 inside the waveguide region and $F_A(F_B)$ and $R_A(R_B)$ inside the arms of the MZ modulator are connected together using the following boundary conditions:

$$F_A(z_s, t) = F_B(z_s, t) = \frac{1}{\sqrt{2}} F_2(z_s, t) \quad (11a)$$

$$R_A(z_s, t) + R_B(z_s, t) = R_2(z_s, t). \quad (11b)$$

In (11), it is assumed that the Y-splitter is an ideal 50:50 MMI splitter with no insertion loss.

There are two possible arrangements for the output coupler of the MZ modulators; they are the 2×1 and 2×2 MMI output couplers. The MZ modulator using a 2×1 MMI coupler can be further divided into two types—symmetric and asymmetric. The

main difference between symmetric and asymmetric MZ modulators is that the former has waveguide arms of equal length while the latter has arm lengths intentionally mismatched by ΔL in order to obtain a π -phase-shifted MZ between both arms at zero bias voltage [4], [5]. In our model, ΔL can be implemented by adjusting the relative value of $\Delta\beta$ between both arms, that is, $\pi = (\Delta\beta_A - \Delta\beta_B) \times L_{MZ}$ at a zero bias voltage but the optical length of both arms remain unchanged in the model. Similarly, for the 2×2 MZ modulator, the required ΔL can be implemented by adjusting $\Delta\beta$ between both arms to realize a $\pi/2$ phase-shift.

For the 2×1 MZ modulator, the forward and reverse fields, $F_A(F_B)$ and $R_A(R_B)$ as well as F_3 and R_3 , at the Y-combiner junction (i.e., $z = z_e$) can be written as

$$R_A(z_e, t) = R_B(z_e, t) = \frac{1}{\sqrt{2}} R_3(z_e, t) \quad (12a)$$

$$F_A(z_e, t) + F_B(z_e, t) = F_3(z_e, t). \quad (12b)$$

Equation (12) is deduced using the same assumptions in the derivation of (11). At the facet of the modulator (i.e., $z = z_r$), the boundary condition is given by

$$R_3(z_r, t) = r_R F_3(z_r, t) \quad (13)$$

where $r_R (= |r_R| \exp(j\phi_R))$ is the reflectivity of the right facet of the 2×1 MZ modulator and ϕ_R is the corresponding facet phase.

For the 2×2 MZ modulator, the forward and reverse fields, $F_A(F_B)$ and $R_A(R_B)$ as well as $F_{TA}(F_{TB})$ and $R_{TA}(R_{TB})$, at the Y-combiner/splitter junction (i.e., $z = z_e$) can be written as [9]

$$\begin{bmatrix} F_{TA}(z_e, t) \\ F_{TB}(z_e, t) \end{bmatrix} = \frac{1}{\sqrt{2}} \begin{bmatrix} 1 & -j \\ -j & 1 \end{bmatrix} \begin{bmatrix} F_A(z_e, t) \\ F_B(z_e, t) \end{bmatrix} \quad (14a)$$

$$\begin{bmatrix} R_A(z_e, t) \\ R_B(z_e, t) \end{bmatrix} = \frac{1}{\sqrt{2}} \begin{bmatrix} 1 & -j \\ -j & 1 \end{bmatrix} \begin{bmatrix} R_{TA}(z_e, t) \\ R_{TB}(z_e, t) \end{bmatrix}. \quad (14b)$$

At the facet of the modulator (i.e., $z = z_r$), the boundary conditions are given by

$$R_{TA}(z_r, t) = r_{RA} F_{TA}(z_r, t) \quad (15a)$$

$$R_{TB}(z_r, t) = r_{RB} F_{TB}(z_r, t) \quad (15b)$$

where r_{RA} and r_{RB} are the facet reflectivities at the branches A and B , respectively, of the 2×2 output coupler. It is also assumed that ϕ_{RA} and ϕ_{RB} are the corresponding phases of the output facets such that $r_{RA} = |r_{RA}| \exp(j\phi_{RA})$ and $r_{RB} = |r_{RB}| \exp(j\phi_{RB})$. Hence, the theoretical models applied to 2×1 and 2×2 MZ modulators are almost the same except for the phase difference between both arms and the boundary conditions of the output couplers of the MZ modulators.

D. Time-Domain Traveling-Wave Method

The time-dependent coupled wave equations can be easily solved using the time-domain traveling-wave algorithm by considering the boundary conditions among the laser, waveguide, and MZ modulator sections [14]. It can be assumed that the entire device is subdivided into small equal subsections and each subsection has an optical length of Δz as shown in Fig. 2(a). It must be noted that, although both arms of the MZ modulator may have a different physical length, the time-domain algorithm restricts them to have the same optical length. The difference in the physical length between the two arms can be taken into consideration by introducing an equivalent phase shift into the traveling-wave equation through $\Delta\beta$. For the laser section, it is assumed in Fig. 2(a) that there are n sets of g , $\Delta\beta$, U_f , and U_r , which are uniformly distributed inside each subsection but nonuniformly distributed over the entire laser cavity. In addition, there are $n + 1$ pairs of F_1 and R_1 allocated at the edges of each subsection of the laser section such that the nonuniform distribution of the traveling waves can be described in a discrete way. Other sections can also be described in a similar manner.

Fig. 2(b) shows the corresponding schematic of the self-consistent calculation of a two-dimensional (2-D) and one-dimensional (1-D) numerical integration of (1) and (7), respectively, for the laser and waveguide sections. It must be noted that the traveling waves between subsections are con-

TABLE I
PARAMETERS FOR THE DFB LASER INTEGRATED WITH AN MZ MODULATOR

Description	Symbol	Value
wavelength	λ_R	1.56 μm
length of laser	L	300 μm
length of modulator	L_{MZ}	600 μm
length of waveguide (MMI splitter)	L_{WG1}	100 μm
length of waveguide (MMI combiner/splitter)	L_{WG2}	200 μm
amplitude of reflection between laser & WG	r_{LM}	0.0
coupling coefficient of DFB laser	κ	50 cm^{-1}
group refractive index	n_g	3.7
gain coefficient of QW materials	a_N	1500 cm^{-1}
confinement factor in transverse direction	Γ	0.35
spontaneous emission factor	β_s	1×10^{-4}
Bimolecular carrier coefficient	B_{sp}	$1 \times 10^{-10} \text{ cm}^3 \text{ s}^{-1}$
material loss	α_c	20 cm^{-1}
gain compression factor	ϵ	$4 \times 10^{-17} \text{ cm}^{-3}$
carrier density at transparency	N_t	$1.5 \times 10^{18} \text{ cm}^{-3}$
linewidth enhancement factor	α_H	4.0
initial carrier concentration	N (at $t=0$)	$2 \times 10^{18} \text{ cm}^{-3}$
thickness of active layer	d	0.01 μm

nected together through (1) and this is obtained by expressing (1) in the following format [14]:

$$\begin{aligned} F(z + \Delta z, t + \Delta t) - F(z, t) \\ \approx \Delta z \left[\left(\frac{1}{2} \Gamma g + j \Delta \beta \right) F(z, t) + j k R(z, t) + U_f(t, z) \right] \end{aligned} \quad (16a)$$

$$\begin{aligned} R(z - \Delta z, t + \Delta t) - R(z, t) \\ \approx \Delta z \left[\left(\frac{1}{2} \Gamma g + j \Delta \beta \right) R(z, t) + j k F(z, t) + U_r(t, z) \right] \end{aligned} \quad (16b)$$

where the relation between the time and spatial steps in the longitudinal direction, $\Delta z = \nu_g \Delta t$, has been applied to derive (16). By knowing the initial field values at time t_o , the forward (reverse) field at the next time step $t_o + \Delta t$ ($\Delta t = \Delta z / \nu_g$) can be determined at the node $z + \Delta z$ ($z - \Delta z$) from (1). The device's parameters, such as g , $\Delta\beta$, U_f , and U_r , as well as the boundary conditions, are applied to the nodes. For example, at the interface $z = z_f$, the forward and reverse fields between the laser and waveguide sections are matched through the boundary condition (10). As indicated in Fig. 2(b), the optical fields F_1 and R_1 should also match with F_2 and R_2 at the right time. This time-domain boundary condition should also be maintained throughout the device's entire cavity. In fact, this is the most important issue to be satisfied in the time-domain traveling-wave algorithm. Furthermore, by knowing the initial value of carrier concentration, the carrier concentration at the next time step can also be determined using the following approximation:

$$N(t_o + \Delta t) \approx N(t_o) + \left. \frac{\partial N}{\partial t} \right|_{t=t_o} \Delta t. \quad (17)$$

Hence, the implementation of the laser-MZ modulator is simple and straightforward.

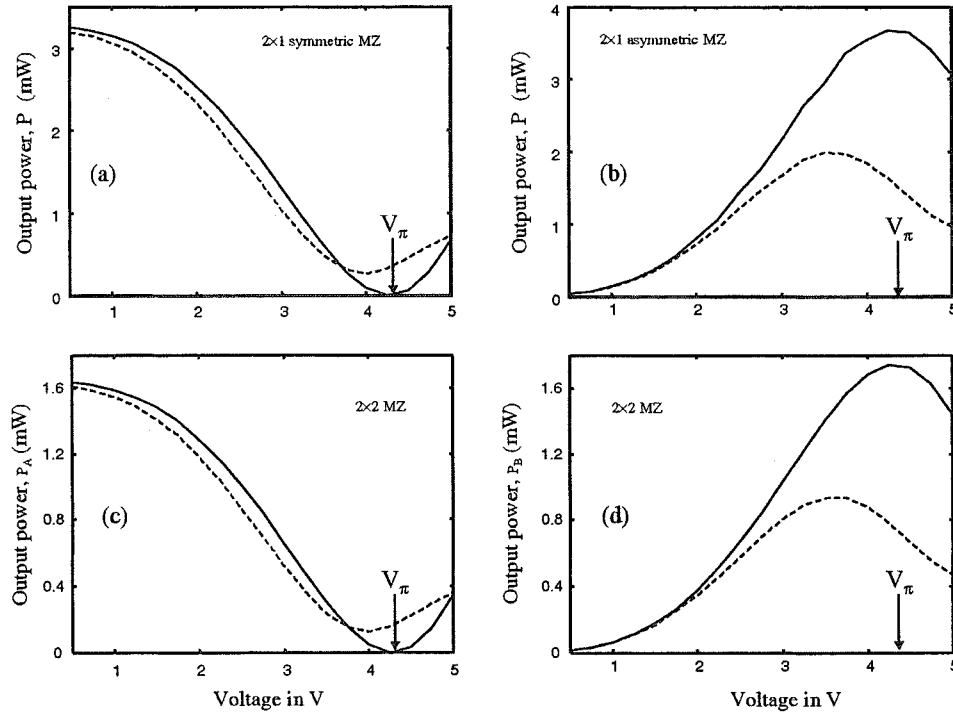


Fig. 3. Output power of the integrated laser-MZ modulator under the variation of the reverse bias voltage. The dashed lines correspond to the case $\Delta_{MA}\alpha = 0$ and the solid lines correspond to (8a) and (8b). (a) A 2×1 symmetric MZ modulator. (b) A 2×1 asymmetric MZ modulator. (c), (d) The output optical power from the splitter's branches *A* and *B*, respectively, of a 2×2 MZ modulator.

The key steps to realizing the time-domain traveling-wave algorithm for the laser-MZ modulator can be summarized below.

- In order to analyze the longitudinal field distribution inside the device, the laser, waveguide, and MZ sections are divided into a number of subsections, which should have the same optical length, Δz .
- In the time-domain algorithm, both arms of the MZ modulator should have the same optical length. The actual difference in their physical length can be simulated by alternating $\Delta\beta$ between both arms. Hence, any phase shift of a 2×1 or 2×2 MZ modulator can be implemented using the time-domain traveling-wave algorithm.
- The forward and reverse fields at all boundaries between the laser, waveguides, and MZ modulator should also be matched in time.
- It is required that the rate equation of the carrier concentration and the time-dependent coupled wave equation are solved simultaneously in a self-consistent manner.

III. NUMERICAL CALCULATIONS

In the first part of this section, our proposed time-domain traveling-wave model is verified by repeating the calculation on the static and small-signal modulation response of the integrated laser-MZ modulator given in [9]. In the other parts of this section, the large-signal dynamic responses of MZ modulators are studied using the proposed model for the first time. It is shown that the turn-on and -off frequency chirps (i.e., adiabatic chirp) under the influence of residual optical feedback can be minimized using a suitable configuration of the MZ modulator. In addition, the chirped frequency spikes (i.e., transient chirp), due to

the rapid variation of electrical signal, induces refractive index change in the MZ modulators, can broaden the linewidth, and distort the spectrum of the modulated optical signal. Furthermore, a dual-arm dual-signal modulation format is suggested to double the modulation speed of the MZ modulators. In the following calculation, the parameters for the laser, waveguide, and MZ modulator are shown in Table I. In addition, (8a) and (8b) are used to model the small change of the optical absorption and refractive index of the MZ modulator under the control of the reverse bias voltage [9]. Other device parameters that have not been mentioned will be given accordingly.

A. Example: Static and Small-Signal Modulation Response of the MZ Modulator

The time-domain traveling-wave model of MZ modulator is examined by checking the corresponding variation of steady-state output power with a reverse bias voltage applied on arm-*A*. Fig. 3(a)–(d) shows the output power versus the reverse bias voltage for the following cases: (a) an MZ modulator with a symmetric 2×1 MMI output coupler; (b) an MZ modulator with an asymmetric (π -shifted) 2×1 output coupler; (c) an MZ modulator with branch “*A*” of the 2×2 ($\pi/2$ -shifted) output coupler; and (d) an MZ modulator with branch “*B*” of the 2×2 ($\pi/2$ -shifted) output coupler. In the calculation, it is assumed that the laser is biased such that the steady-state output power is around 5 mW before entering the MZ modulator. In order to single out the steady-state response of the MZ modulators, the influence of the residual optical feedback from the output facet of the MZ modulators is ignored.

In the figures, the corresponding artificial case $\Delta\alpha_{MZ} = 0$ is also plotted by the solid line for comparison purposes. It is noted

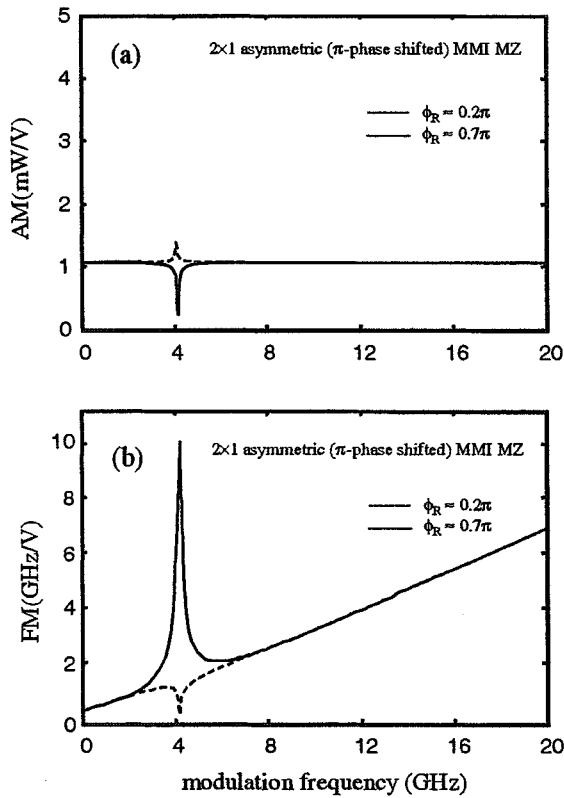


Fig. 4. (a) AM and (b) FM of an asymmetric 2×1 MZ modulator. The solid and dashed lines are the results of the MZ modulator with a facet phase of 0.2π and 0.7π , respectively.

that, for the case of $\Delta\alpha_{MZ} = 0$, it is found that the reverse bias voltage for a π -phase shift between arm-*A* and -*B*, V_π , is about 4.25 V, which was indicated in Fig. 3. It is observed that, for the cases $\Delta\alpha_{MZ} \neq 0$, both symmetric 2×1 and 2×2 (output from branch-*A*) MMI couplers [i.e., Fig. 3(a) and (c), respectively] have similar characteristics but both present a lower extinction ratio due to the nonzero output power at V_π . On the other hand, the asymmetric 2×1 and 2×2 (output from branch-*B*) MMI couplers [i.e., Fig. 3(b) and (d), respectively], which have similar characteristics, have a higher extinction ratio, as the output power is almost zero at a reverse bias voltage of 0.5 V. This is because, for the case $\Delta\alpha_{MZ} \neq 0$, the minimum output optical power never goes to zero nor is the value of the maximum power greater than that for the case when $\Delta\alpha_{MZ} = 0$. Thus, the proposed time-domain traveling-wave algorithm has shown that these steady-state results are consistent with those given in [9].

The AM and FM responses of MZ modulators can also be obtained by applying a small electrical impulse on top of the dc bias to the arm-*A* electrode. The spontaneous emission noise is switched off inside the laser section in order to obtain a clean modulation response. Hence, the Fourier transform of the amplitude and phase of the optical field gives the AM and FM responses, respectively, of the MZ modulator. In our calculation, a π -phase-shifted 2×1 MZ modulator with $|r_L| = 0.9$, $\phi_L = 0$, $|r_R| = \sqrt{2} \times 10^{-4}$, and a dc reverse bias voltage of 2.5 V are used. In addition, the laser is biased such that the steady-state output power from the laser section before entering the MZ modulator is around 5 mW. Fig. 4 plots the AM and FM

responses of the MZ modulator for some values of ϕ_R . It is observed that the AM response exhibits a peak or notch (i.e., at the resonance frequency of the laser) depending on the value of ϕ_R . Similar behavior is also observed in the plot of the FM response. These results are due to the in-phase and out-of-phase between the laser and modulator through the difference between ϕ_L and ϕ_R [9]. From Fig. 4, we conclude that the proposed time-domain traveling-wave algorithm can produce a small-signal modulation response of MZ modulators, and these results are consistent with those given in [9].

B. Large-Signal Modulation Response of an Asymmetric 2×1 MZ Modulator

One of the advantages of our proposed model over the others [7]–[9] is that the large-signal dynamic response of the integrated laser-MZ modulator can be studied. This can be realized by modulating the MZ modulator with square electrical pulses. In order to minimize any abrupt change in the square electrical pulses, a more realistic electrical signal is modeled using a Gaussian function, which is written as [15]

$$V(t) = \begin{cases} 0, & t < 0 \\ V_p(1 - \exp(-t^2/\tau_{RC}^2)) & 0 \leq t < T_p \\ V_p \exp(-(t - T_p)^2/\tau_{RC}^2), & t \geq T_p \end{cases} \quad (18)$$

where $V_p = 3.5$ V, T_p is the pulsewidth, and τ_{RC} is the time constant. It is noted from (18) that $V(t)$ may exhibit a steep change at time $t = 0$ and $t = T_p$ if τ_{RC} is too small (i.e., less than 20 ps). Fig. 5(a) shows the corresponding voltage waveform used to drive the modulator. A sequence of electrical square pulses (with T_p equal to 0.5 or 1.5 ns and $\tau_{RC} = 25$ ps) is used to modulate the π -phase-shifted 2×1 MZ modulator. In the calculation, it is assumed that $|r_L| = 0$, $\phi_L = 0$, $|r_R| = \sqrt{2} \times 10^{-4}$ (i.e., represents the residual optical feedback from the modulator's facet with an antireflection coating) and $\phi_R = 0$. In addition, the steady-state power emitted from the laser before entering the MZ section is maintained around 5 mW. Fig. 5(b) shows the optical output, which exhibits relaxation oscillations, from the MZ modulator. This is expected because the residual optical feedback at the output facet of the MZ modulator induces relaxation oscillations [10]. The frequency chirp of this output signal can also be calculated from the instantaneous frequency, which is given by [10]

$$\omega(t) = \frac{\partial \phi_3}{\partial t} \equiv \text{Imag}(\log(F_3(z_3))) \quad (19)$$

where ϕ_3 is the phase of the optical field F_3 at the output facet of the MZ modulator and $\text{Imag}(\cdot)$ stands for the imaginary part. In the calculation of frequency chirp, the spontaneous emission noise is switched off from the laser section in order to obtain a noise free frequency chirp response. Fig. 5(c) shows the corresponding frequency chirp response of the MZ modulator. Chirped frequency spikes are observed at the time when $V(t)$ is just turned on and off. The steep change in $V(t)$ induces a rapid variation in refractive index [i.e., through (8b)] inside the MZ modulator and as a result chirped frequency spikes are excited. In fact, our calculation given in Fig. 5(c) is correct and the large magnitude of the chirped frequency spikes is due to: 1) a steep change in $V(t)$ and 2) the change in phase of optical field

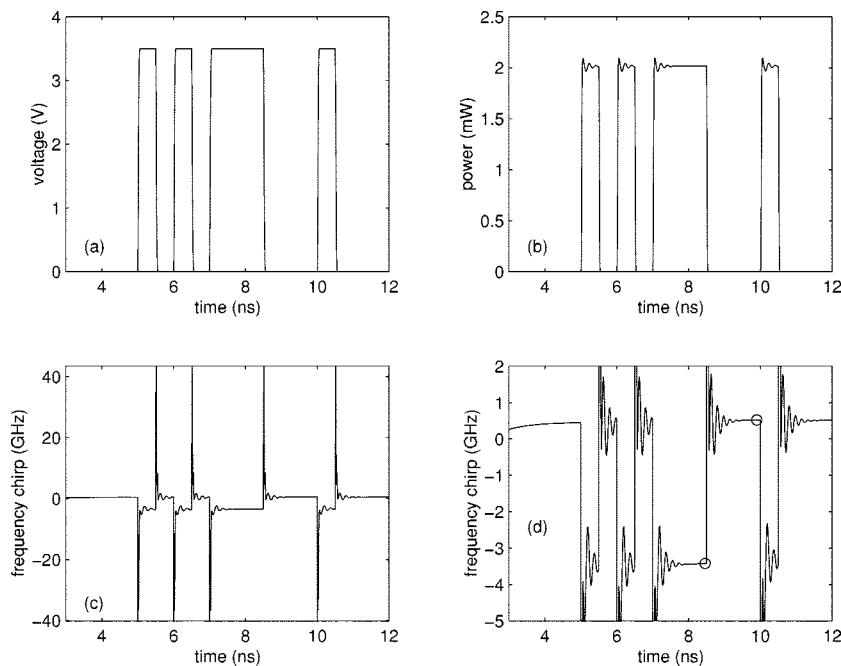


Fig. 5. Large-signal dynamic response of an asymmetric 2×1 MZ modulator ϕ_R , equal to zero. (a) Reverse bias voltage. (b) Output power. (c) Frequency chirp response. (d) Enlargement of the frequency chirp response of (c).

is a strong function of $V(t)$. In a practical situation, the steep change in $V(t)$ will be smoothed out such that the chirped frequency spikes will have a smaller magnitude. It can be shown that increasing the value of τ_{RC} (say to 100 ps) can smooth out the steep change in $V(t)$ and a more reasonable peak magnitude of the chirped frequency spikes (i.e., about ± 9 GHz) can be obtained. In order to study the influence of chirped frequency spikes on the spectrum of the optical signal under large-signal modulation, the driving signal with a rapid variation of electrical waveform (i.e., $\tau_{RC} = 25$ ps) will still be used in other sections of this paper.

Fig. 5(d) shows the enlargement of Fig. 5(c). Apart from the chirped frequency spikes, the frequency chirp response exhibits relaxation oscillations, which are also induced by the residual optical feedback at the output facet of the MZ modulator. A frequency chirp difference during the “on” and “off” states are “ ω_{on} ” and “ ω_{off} ”, respectively, as indicated by “o” on the diagram. This difference illustrates the change in lasing frequency caused by the residual optical feedback from the modulator facet. Fig. 6 shows the variation of “ ω_{on} ” and “ ω_{off} ” by varying ϕ_R from 0 to 2π . It is noted that the frequency chirp at the turn-on state, ω_{on} , is strongly dependent on the facet phase, ϕ_R , of the MZ modulator. This is because at the turn-off state destructive interference occurs at the MZ modulator and only a very small amount of light is reflected back to the DFB laser. It is also noted that the phase of the residual optical feedback has no influence on the peak magnitude of the chirped frequency spikes.

C. Large-Signal Response of a $\pi/2$ -Shifted 2×2 MZ Modulator

The large-signal modulation response of a $\pi/2$ -shifted 2×2 MZ modulator is analyzed here. It is assumed that $|r_L| = 0$, $\phi_L = 0$, $|r_{RB}| = \sqrt{2} \times 10^{-4}$, $\phi_{RB} = 0$, and

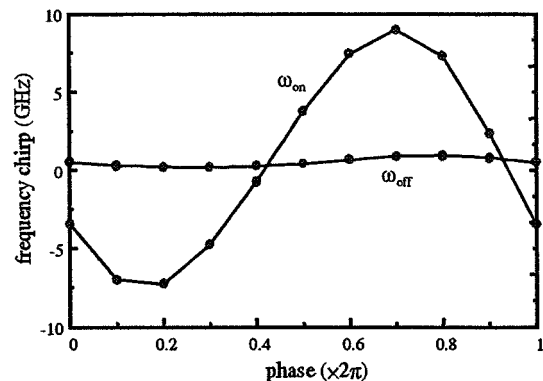


Fig. 6. Variation of turn-on and turn-off frequency chirps (i.e., ω_{on} and ω_{off}) with ϕ_R for the asymmetric 2×1 MZ modulator.

$|r_{RA}| = \sqrt{2} \times 10^{-4}$. ϕ_{RA} can be varied between 0 and 2π . The reverse bias voltage used in Fig. 5(a) is applied to study the large-signal dynamic response of the $\pi/2$ -shifted 2×2 MZ modulator. This is because we would like to single out the influence of the chirped frequency spikes on the modulated optical signal in the frequency domain. Fig. 7(a) and (b) shows the output optical power emitted from branches A and B (i.e., P_A and P_B), respectively, with $\phi_{RA} = 0$. The frequency chirp response of P_A and P_B are also given in Fig. 7(c) and (d), respectively. It is noted that only chirped frequency spikes appear in the plot of the frequency chirp response. The difference between the turn-on and -off frequency chirp is almost negligible (i.e., less than 1 MHz for both P_A and P_B) when compared with that given in Fig. 5(d) (i.e., greater than 14 GHz). This is because the reflected fields experience destructive interference just before reflecting back to the laser section and can be explained from (12) and (14). Supposing R_{TA} is the only optical field reflected back from the output facet ($z = z_r$) to the MZ section, the electric field R_2 at $z = z_s$

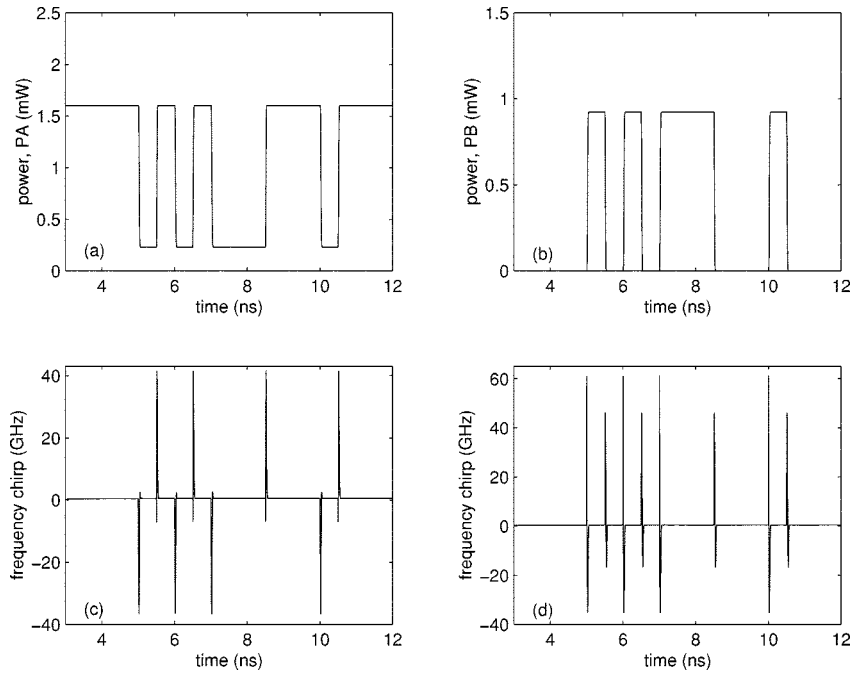


Fig. 7. Large-signal dynamic response of a 2×2 MZ modulator. (a), (b) Output power from the splitter's branches A and B (i.e., P_A and P_B) of the MZ modulator, respectively. (c), (d) Frequency chirp responses of P_A and P_B , respectively.

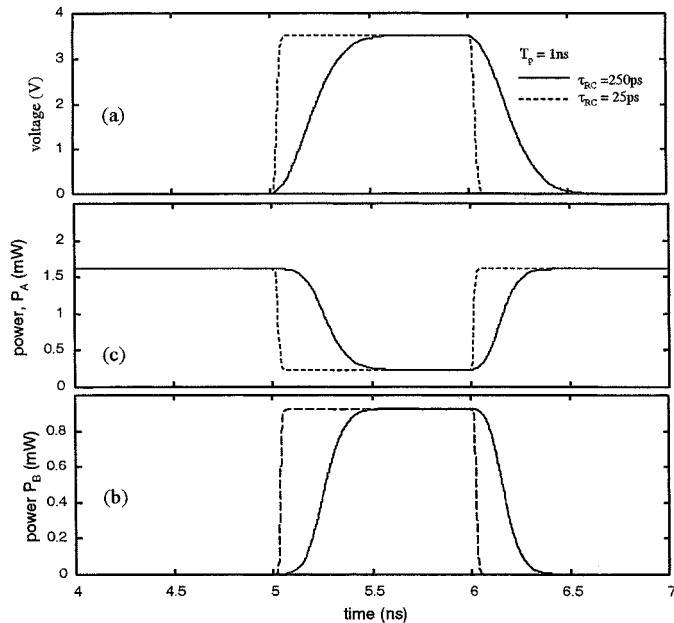


Fig. 8. (a) Waveform of electrical pulse, $V(t)$, with $T_p = 2$ ns. (b) Output power from branch- A , P_A and (c) output power from branch- B , P_B of the 2×2 MZ modulator. The dashed line corresponds to $\tau_{RC} = 25$ ps and the solid line corresponds to $\tau_{RC} = 250$ ps.

can be related to R_A and R_B using (12a) and to R_{TA} using (14b), which gives

$$R_2 = R_A e^{j\phi} + R_B = \frac{1}{\sqrt{2}} (R_{TA} e^{j\phi} - jR_{TA}) = 0 \quad (20)$$

where ϕ is the phase difference between arms A and B of the MZ modulator and is equal to $\pi/2$ at both the turn-on and -off states. Hence, the reflected fields will cancel out before entering the laser section for all values of the facet reflectivity and phase. Because of this, ϕ_{RA} is assumed to be zero in the calculation.

As mentioned in the beginning of this section, the influence of chirped frequency spikes on the spectral profile of the optical pulses can be extracted from the large-signal response of the $\pi/2$ -shifted 2×2 MZ modulator. This is because the difference between ω_{on} and ω_{off} is almost negligible when compared with the amplitude of the chirped frequency spikes. Therefore, any broadening and distortion of the modulated optical signal will only be attributed to the presence of the chirped frequency spikes. The spectrum of the modulated optical signal can be calculated by the Fourier transformation of the corresponding optical field in the time domain. Fig. 8 shows the effect of τ_{RC} (dashed line for $\tau_{RC} = 25$ ps and solid line for $\tau_{RC} = 250$ ps) on (a) the voltage waveform, (b) the output optical power from branch A , and (c) the output optical power from branch B of the $\pi/2$ -shifted 2×2 MZ modulator. In the calculation, the voltage pulse is assumed to have $T_p = 1$ ns. The corresponding frequency chirp response and spectrum of the modulated optical pulse from branches A and B are given in Figs. 9 and 10, respectively. In Fig. 9(a) and (c), the frequency chirp responses of P_A for the cases $\tau_{RC} = 250$ and 25 ps, respectively, are given. It is observed that the magnitude of the chirped frequency spikes is reduced if the steep change of electrical signal is minimized (i.e., by increasing the value of τ_{RC}) but the chirped frequency spikes still occur in the frequency chirp response. In Fig. 9(b) and (d), it is shown that the fine structure still appears in the spectrum even though the amplitude of the chirped frequency spikes is reduced. The dashed line given in Fig. 9(b) is the spectrum of the laser output power without modulation. Hence, the excitation of the chirped frequency spikes due to the steep change in $V(t)$ induces an index change, which cannot be avoided (even with large τ_{RC}), in the MZ modulator and will contribute to the broadening and distortion of the spectrum of the modulated optical signal. The frequency chirp response and spectrum profile of P_B , which show characteristics similar to P_A , are also given in Fig. 10.

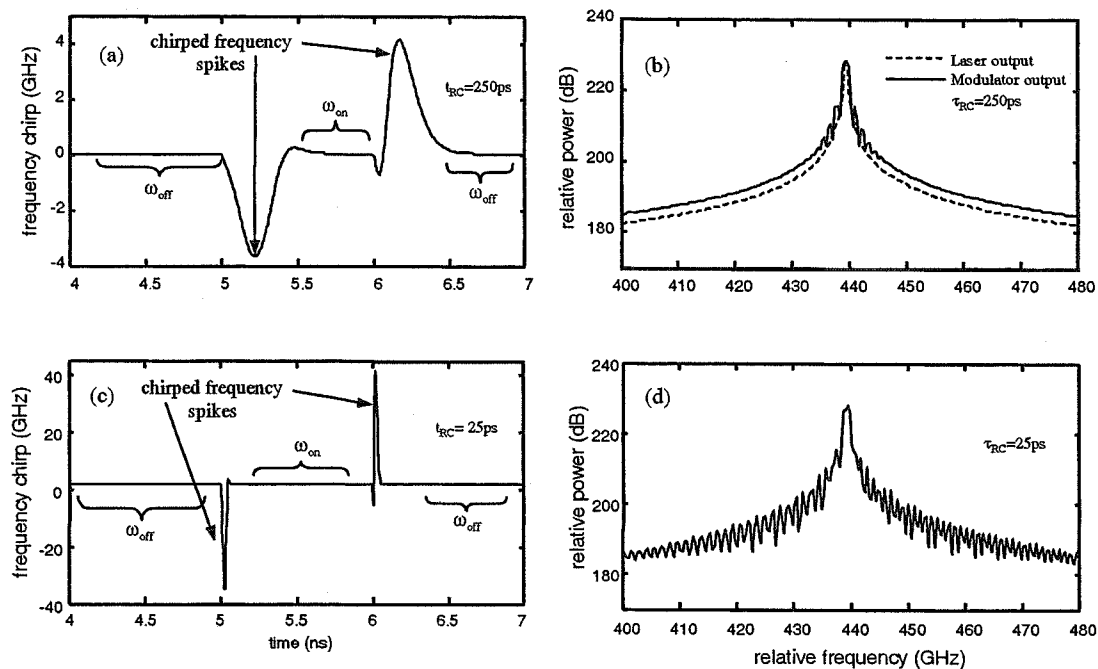


Fig. 9. Optical signal output from branch-A of the 2×2 MZ modulator. (a) Frequency chirp response and (b) spectrum for the case $\tau_{RC} = 250$ ps. (c) Frequency chirp response and (d) spectrum for the case $\tau_{RC} = 25$ ps.

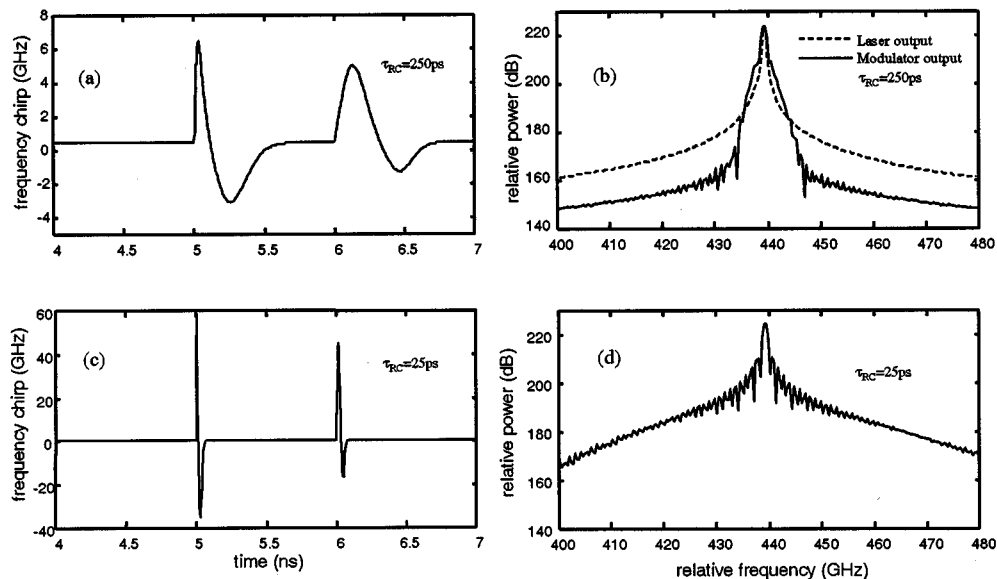


Fig. 10. Optical signal output from branch-B of the 2×2 MZ modulator. (a) Frequency chirp response and (b) spectrum for the case $\tau_{RC} = 250$ ps. (c) Frequency chirp response and (d) spectrum for the case $\tau_{RC} = 25$ ps.

D. Dual-Arm Dual-Signal Modulation of MZ Modulators

The modulation speed of an MZ modulator can be doubled from its driving electrical signal if both arms of the MZ modulator are under dual-signal modulation. That is, the dual electrical signals are identical except with a constant time shifted by one half of a period. Fig. 11 shows the proposed arrangement of the electrical signals input to the MZ modulator. Both triangle-pulse trains with a period of 2 ns, but with a time shift of 1 ns, are applied to both arms of the MZ modulator with a symmetric 2×1 MMI output coupler. It must be noted that, if only one

member of a triangle-pulse train is applied to one arm, the output optical power from the MZ modulator will have the same period (i.e., same modulation speed) as that of the electrical signal. However, if both electrical signals (with a time shift of 1 ns) are applied to different arms of the MZ modulator, the output power from the MZ modulator will have a new period of 1 ns such that the modulation frequency is doubled. Other types of electrical-pulse trains such as those with a Gaussian shape can also be applied to realizing dual-signal modulation provided that the total energy of the electrical signal occupies only one-fourth of the entire period.

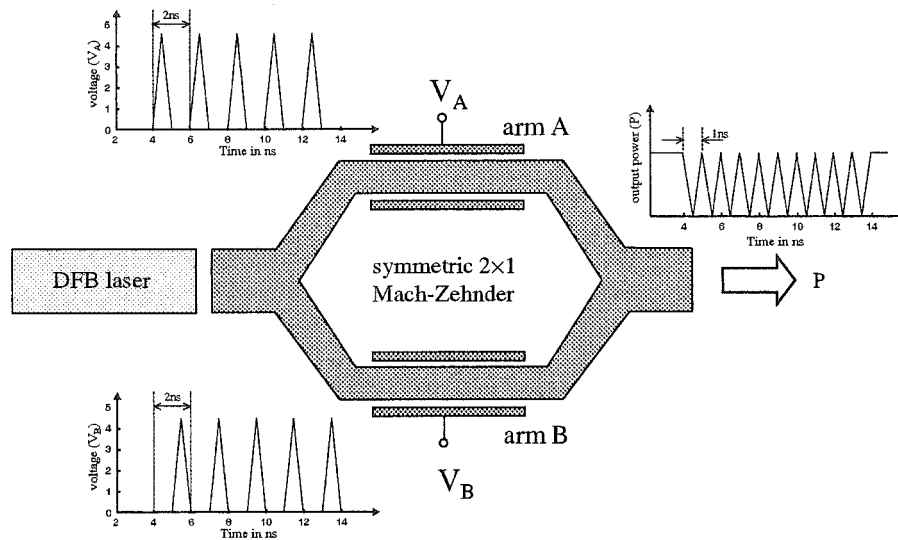


Fig. 11. Schematic diagram of a symmetric 2×1 MZ modulator under dual-arm dual-electrical signal modulation.

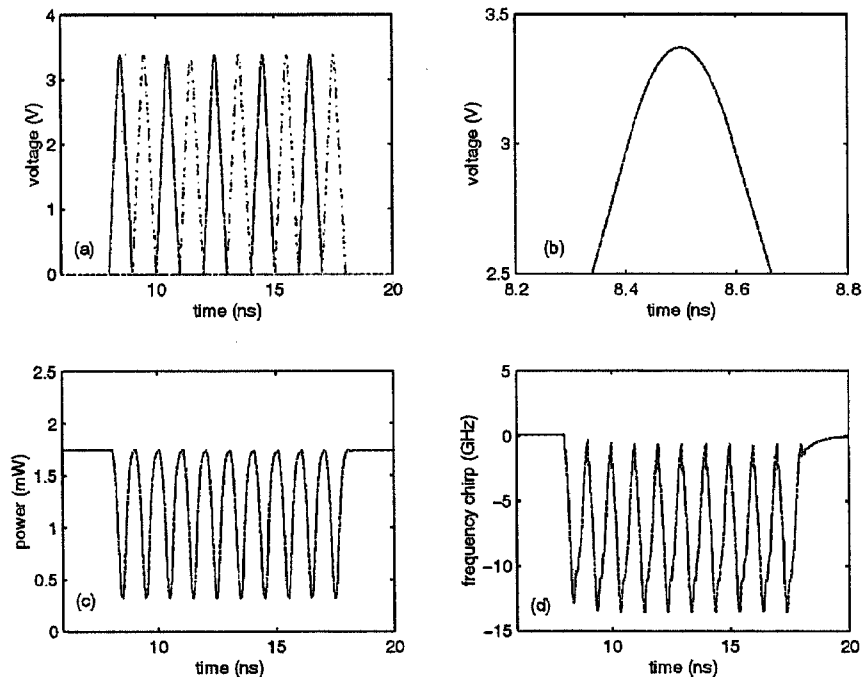


Fig. 12. Large-signal dynamic response of a symmetric 2×1 MZ modulator under dual-arm dual-signal modulation with a facet phase of MZ modulator ϕ_R equal to zero. (a) Reverse bias voltage (solid lines: bias on arm A and dotted-dashed lines: bias on arm B). (b) Enlargement of (a). (c) Output power. (d) Frequency chirp response.

Fig. 12 shows the large-signal dynamic response of a symmetric 2×1 MZ modulator under dual-arm dual-signal modulation with $|r_L| = 0$, $\phi_L = 0$, $|r_R| = \sqrt{2} \times 10^{-4}$ and $\phi_R = 0$ being assumed in the calculation. Fig. 12(a) shows the reverse bias voltage applied on arms A and B and Fig. 12(b) shows the enlargement of the triangle waveform near its peak value. Fig. 12(c) and (d) shows the corresponding optical power and frequency chirp response, respectively. It is observed that no chirped frequency spike occurs in the plot of the frequency chirp. This is mainly due to the shape of the electrical signal where there is no step change in the electrical waveform (i.e., a rapid variation of the refractive index) is introduced. In addition, the maximum variation of the frequency chirp is about

12 GHz, which is compatible with those using square electrical pulses, as shown in Fig. 10(a). In fact, it can be shown that the influence of ϕ_R has no effect on the difference between the maximum and minimum magnitude of the frequency chirp.

The performance of a 2×2 MZ modulator with dual-arm dual-signal modulation is also studied. Arrangement of the input of the electrical signals is similar to that given in Fig. 11. The modulated output optical signal is obtained from branch A of the 2×2 MZ modulator. In the calculation, it is assumed that $|r_L| = 0$, $\phi_L = 0$, $|r_{RB}| = \sqrt{2} \times 10^{-4}$, $\phi_{RB} = 0$, $|r_{RA}| = \sqrt{2} \times 10^{-4}$, and $\phi_{RA} = 0$. It is found that the output power P_A and frequency chirp response exhibit characteristics similar to those given in Fig. 12(c) and (d), respectively. There is no im-

provement in the frequency chirp response because the destructive condition given by (20) cannot be maintained due to the nonuniform variation of the optical power within a pulse period such that R_A and R_B in (20) have different magnitudes. However, the maximum variation of the frequency chirp in a 2×2 MZ modulator is close to that of the 2×1 MZ modulator.

In the above analysis, it is noted that the driven voltage signals are of the return-to-zero format while the modulated output optical signal is of a nonreturn-to-zero format, and this requires an increase in the bandwidth of the modulator. In addition, the extinction ratio in Fig. 12(c) is reduced when compared to that given in Fig. 5. However, our purpose here is to demonstrate the possibility of frequency doubling using the proposed modulation method. It should be noted that, given a sufficiently large bandwidth modulator, our results show that the modulation speed will be doubled and the extinction ratio will not deteriorate. Therefore, frequency doubling can be realized in symmetric 2×1 and 2×2 MMI MZ modulators with dual-arm dual-signal modulation and acceptable frequency chirp.

IV. DISCUSSION AND CONCLUSION

In [9, Fig. 9], it is shown that the 2×1 MMI MZ modulator is less sensitive to residual optical feedback than is the 2×2 type. It seems that the result given in [9] contradicts our results given in Section III (i.e., a 2×2 MMI MZ modulator has much better immunity to residual optical feedback than does the 2×1 type). It must be noted in our analysis that only the frequency chirp difference during the “ON” and “OFF” states (i.e., adiabatic chirp) is immune to residual optical feedback in a 2×2 MMI MZ modulator, but the corresponding magnitude of the chirped frequency spikes (i.e., transient chirp) is larger than that of the 2×1 type. In Fig. 7(d) (2×2 type), the maximum peak-to-peak chirped frequency spike is about 100 GHz, and that given in Fig. 5(c) (2×1 type) is about 80 GHz, which indicates that the transient chirp of a 2×2 MMI MZ modulator is more sensitive to residual optical feedback than that for the 2×1 type. Therefore, our prediction is consistent with that given in [9].

The influence of the interface reflection on the difference in frequency chirp between the turn-on and -off states (i.e., adiabatic chirp) has been analyzed extensively in [8]. For example, the increase in reflection between the laser and modulator interface reduces the adiabatic chirp. This is because a more closed cavity helps shield the laser from the external reflection. Similar results can also be reproduced by our model and hence are not repeated in this paper. For the chirped frequency spikes (i.e., transient chirp), it can be shown that the peak value of frequency chirp spikes is mainly dependent on the driving waveform if the amplitude of external reflection between the laser/MZ modulator is small ($\leq \sqrt{2} \times 10^{-4}$). However, for an increase in the amplitude of external reflection, the peak value of the frequency chirp spikes will be reduced due to the influence of the closed cavity. On the other hand, the influence of reflection at the interface of the Y-junction cannot be analyzed using our proposed model due to the assumptions used in the derivation of (11), (12), and (14).

A simple and powerful large-signal dynamic model for a DFB laser integrated with a MZ modulator has been developed. The computer program has been implemented using a straightforward time-domain traveling-wave algorithm with appropriate

boundary conditions such that models for MZ modulators with 2×1 and 2×2 MMI output couplers can be easily realized. Using the developed time-domain traveling-wave model, the large-signal modulation response of the DFB laser integrated with an MZ modulator has been investigated. It has been found that the adiabatic chirp of a 2×2 MMI MZ modulator is minimal compared with that of a 2×1 type and is independent of the residual optical feedback. This is because the MZ modulator with a $\pi/2$ -shift 2×2 MMI output coupler introduces a destructive interference of the reflected optical fields before they enter the laser section. Furthermore, it has been noted that the excitation of chirped frequency spikes, which are due to the steep variation of the driving waveform and, hence, a change in the refractive index, can broaden and distort the spectrum of the modulated optical signal in an MZ modulator. Therefore, it is desirable to completely remove the chirped frequency spikes from the MZ modulator but this may not be possible because a large-signal modulation will always have a rapid variation in the refractive index inside the MZ modulator. Even the magnitude of the chirped frequency spikes is suppressed using an electrical waveform with a less steep change, and broadening and distortion of the spectrum of the modulated optical signal are still observed. On the other hand, the dual-arm dual-signal modulation format has been applied to double the modulation speed of MZ modulators. It has been found that for both asymmetric 2×1 and 2×2 MMI MZ modulators, the modulation frequency of the optical signal can be doubled using triangular electrical pulses. In addition, the chirped frequency spike is negligible due to the shape of the electrical pulses and the corresponding frequency chirp response is compatible with that for electrical pulse modulation.

REFERENCES

- [1] Ph. Delansay, S. Gauchard, H. Helmers, D. Penninckx, S. Gurib, and F. Brillouet, “2.5Gbit/s transmission over 1086km of standard single mode fiber using an integrated laser Mach-Zehnder modulator,” in *Proc. Conf. Optic. Fiber Commun.*, San Jose, CA, 1998, paper Tu17.
- [2] D. M. Adams, C. Rolland, A. Fekecs, D. McGham, A. Somani, S. Bradshaw, M. Poirier, E. Dupont, E. Cremer, and K. Anderson, “1.55 μ m transmission at 2.5Gbit/s over 112km of NDSF using discrete and monolithically integrated InGaAsP/OnP Mach-Zehnder modulator and DFB lasers,” *Electron. Lett.*, vol. 34, pp. 771–773, 1998.
- [3] L. Lestra and P. Brosson, “Design rules for a low chirp integrated DFB laser with an electroabsorption modulator,” *IEEE Photon. Technol. Lett.*, vol. 8, pp. 990–1000, Aug. 1996.
- [4] J. Yu, C. Rolland, D. Yevick, A. Sommani, and S. Bradshaw, “Phase engineering III-V MQW Mach-Zehnder modulators,” *IEEE Photon. Technol. Lett.*, vol. 8, pp. 1018–1020, 1996.
- [5] D. Penninckx, Ph. Delansay, E. Boucherez, C. Fortin, and O. Gouezigou, “InP/GaInAsP π -phase shifted Mach-Zehnder modulator for wavelength independent (1530–1560nm) propagation performance at 10Gbit/s over standard dispersive fiber,” *Electron. Lett.*, vol. 33, pp. 697–698, 1997.
- [6] D. Penninckx and Ph. Delansay, “Comparison of the propagation performance over standard dispersive fiber between InP based π -phase shifted and symmetric Mach-Zehnder modulators,” *IEEE Photon. Technol. Lett.*, vol. 9, pp. 1250–1252, 1997.
- [7] J. C. Cartledge, C. Rolland, S. Lemerle, and A. Solheim, “Theoretical performance of 10Gb/s lightwave systems using a III-V semiconductor Mach-Zehnder modulator,” *IEEE Photon. Technol. Lett.*, vol. 6, pp. 282–284, Feb. 1994.
- [8] X. Li, W. P. Huang, D. M. Adams, C. Rolland, and T. Makino, “Modeling and design of a DFB laser integrated with a Mach-Zehnder modulator,” *IEEE J. Quantum Electron.*, vol. 34, pp. 1807–1815, Oct. 1998.
- [9] Ph. Brosson and Ph. Delansay, “Modeling of the static and dynamic responses of an integrated laser Mach-Zehnder modulator and comparison with an integrated EA modulator,” *J. Lightwave Technol.*, vol. 16, pp. 2407–2418, Dec. 1998.

- [10] L. M. Zhang and J. E. Carroll, "Semiconductor 1.55 μ m laser source with gigabit/second integrated electroabsorptive modulator," *IEEE J. Quantum Electron.*, vol. 30, pp. 2573–2577, 1994.
- [11] A. J. Lowery, "New dynamic model for multimode chirp DFB semiconductor lasers," *Proc. Inst. Elect. Eng.*, pt. J, vol. 137, pp. 293–300, 1990.
- [12] D. Marcuse and T. H. Wood, "Simulation of a laser modulation driven by NRZ pulses," *J. Lightwave Technol.*, vol. 14, pp. 860–866, 1996.
- [13] Y. Kim, H. Lee, J. Lee, J. Han, T. W. Oh, and J. Jeong, "Chirp characteristics of 10Gb/s electroabsorption modulator integrated DFB lasers," *IEEE J. Quantum Electron.*, vol. 36, pp. 900–908, Aug. 2000.
- [14] L. M. Zhang, S. F. Yu, M. C. Nowell, D. D. Marcenac, J. E. Carroll, and R. G. S. Plumb, "Dynamic analysis of radiation and side mode suppression in second order DFB lasers using time-domain large-signal traveling wave model," *IEEE J. Quantum Electron.*, vol. 30, pp. 1389–1395, June 1994.
- [15] J. C. Cartledge and G. S. Burley, "The effect of laser chirping on light-wave system performance," *J. Lightwave Technol.*, vol. 7, pp. 568–573, Mar. 1989.



S. F. Yu received the B.E. degree (first class Honors) in electronic engineering from London University, University College, U.K., in 1990 and the Ph.D. degree in optoelectronics engineering from Cambridge University, Robinson College, U.K., in 1993.

He joined the Department of Electronic Engineering, Sha Tin Technical Institute, Hong Kong, as a part-time lecturer in 1993. In 1994, he joined the Department of Electrical and Electronic Engineering, The University of Hong Kong, where he was a Lecturer. Since 1996, he has been an Assistant Professor

in the same department of The University of Hong Kong. In 2000, he worked at Agere System (formerly Lucent Technologies Inc., Optoelectronic Centre, Breinigsville PA) as a member of technical staff. In 2001, he joined the School of Electrical and Electronic Engineering, Nanyang Technological University, Singapore as an Assistant Professor. His main research interest includes the fundamental study, optimization, and practical applications of semiconductor lasers. He conducts research of high-performance semiconductor lasers using diffused quantum-well materials for the application in long-haul optical fiber communication systems. In addition, he contributes to the design and analysis of high-power semiconductor pumped lasers. He is also involved in the development of novel mid-infrared vertical-cavity surface-emitting lasers using quantum cascade architecture and their applications in the measurement of gas and liquid concentrations. Furthermore, he studies the possibilities of using organic materials to fabricate integrated optoelectronics circuit including lasers, modulators, and photodetectors for industrial applications. He has published over 75 international technical papers including invited conference and journal papers, two book chapters, and one book. He also awarded government research funding of total about HK\$3.5 million to support his research activities in the University of Hong Kong.

Dr. Yu was awarded the traditional Departmental Prize by the Department of Electronics and Electrical Engineering, University College London, in the final year degree examination. He was a Fellow and Honorary Scholar of Cambridge Commonwealth Trust Society. He also held a Croucher Foundation scholarship and an overseas research student award while studying for the doctoral program. He is a member of the SPIE. He was a member of the executive committee and was the seminar program chair of the seminar and meeting committee of SPIE Hong Kong Chapter. His biography was published in the 4th edition of *Who's Who in Science and Engineering* (Marquis, USA), the 25th edition of *Dictionary of International Biography*, and the 17th edition of *International Directory of Distinguished Leadership*.



N. Q. Ngo (M'92) received the B.Eng. and Ph.D. degrees in electrical and computer systems engineering from Monash University, Melbourne, Australia, in 1992 and 1998, respectively. During his Ph.D. work, he designed several novel fiber-optic signal processors and integrated optical devices for applications in optical computing and optical fiber communication systems.

From July 1997 to July 2000, he was a Lecturer at Griffith University, Queensland, Australia, where he was director and founder of the Fiber Optic Communications Research Laboratory and conducted research in integrated optics. Since July 2000, he has been an Assistant Professor with Nanyang Technological University, Singapore. His current research interests are fiber Bragg grating devices, sol-gel photonics, microwave photonics, and fiber optic communications. He has been an active reviewer for several international journals.

Dr. Ngo was the recipient of the Douglas Lampard Electrical Engineering Research Prize and Medal from Monash University in 1998, and the Electrical College Prize from the Institution of Engineers, Australia, in 1999, both for his Ph.D. dissertation.